ACS APPLIED MATERIALS & INTERFACES

Research Article

www.acsami.org

Porous Fluorinated SnO_2 Hollow Nanospheres: Transformative Self-assembly and Photocatalytic Inactivation of Bacteria

Shengwei Liu,[†,‡] Guocheng Huang,[†] Jiaguo Yu,*[,‡] Tsz Wai Ng,[†] Ho Yin Yip,[†] and Po Keung Wong*[,†]

[†]School of Life Sciences, The Chinese University of Hong Kong, Shatin, NT, Hong Kong SAR, People's Republic of China

[‡]State Key Laboratory of Advanced Technology for Materials Synthesis and Processing, Wuhan University of Technology, Luoshi Road 122#, Wuhan 430070, People's Republic of China

Supporting Information

ABSTRACT: Highly porous surface fluorinated SnO_2 hollow nanospheres (SnO_2(F) HNS) were produced in high yield by a hydrothermal treatment of stannous fluoride in the presence of hydrogen peroxide. Two important processes in terms of oriented self-assembly and in situ self-transformation were highlighted for the formation of as-prepared SnO_2(F) HNS, which were largely relying on the directing effects of selected specific chemical species in the present synthesis system. Significantly, these SnO_2(F) HNS showed considerable activity in photocatalytic inactivation of a surface negatively charged bacterium, *Escherichia coli* K-12, in aqueous saline solution. The dominant reactive species involved in the inactivation process were also identified.

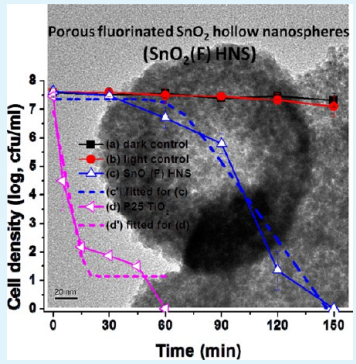

KEYWORDS: *SnO_2 hollow nanospheres, formation mechanism, selective adsorption, bacterial inactivation, scavenger study*

1. INTRODUCTION

Hollow inorganic micro/nanostructures have received great attention recently.[1,2] The technologically important applications, for example, gas sensors, lithium rechargeable batteries, photocatalysts, etc., have stimulated the search for new synthetic methodologies for large-scale synthesis of specific SnO_2 hollow micro/nanostructures.[3−7] Various spherical hard and soft templates, including polystyrene spheres, carbon spheres and silica spheres, have been employed to direct the formation of hollow SnO_2 spheres.[8−10] Also, ellipsoidal α-iron oxide and cuprous oxide nanocubes have been used to synthesize nonspherical hollow SnO_2 structures.[11,12] Templating is a versatile technique to tailor hollow structures. However, it usually involves multiple steps, which are relatively complex and less reproducible, making the scale-up of synthesis difficult. Alternatively, some novel template-free methods[3,13−15] to create hollow structures have been exploited based on specifically proposed chemical mechanism, which attracted great attention and inspired further investigations. For instance, Lou et al. synthesized hollow SnO_2 nanospheres using potassium stannate as a precursor, and proposed that inside-out Ostwald ripening accounted for the hollowing formation.[3] Yang et al. discovered the emergent formation of hollow SnO_2 octahedra, and the formation mechanism was proposed as consecutive three-dimensional oriented self-assembly of primary nanoparticles.[16] Unfortunately, most available template-free synthetic protocols still suffer from the limited structural control and narrow synthetic window, and they, with no exception, are still far from generalized schemes for synthesizing a wide range of hollow materials. Recently, we have developed a facile one-pot template-free method, termed as chemically induced self-transformation (CIST), for the synthesis of a variety of inorganic hollow structures.[17−21] Nevertheless, the underlying chemical mechanism of CIST processes are not yet completely established. An enrichment of synthetic examples related to CIST method and advanced understanding of the synthetic processes and mechanisms are highly desirable and yet challenging.

Disinfection is an indispensable step for water treatment, and photocatalytic water disinfection (PWD) is one of the most promising green technologies.[22−26] Among others, searching for suitable photocatalysts for PWD is essential.[27,28] The photocatalytic materials with hollow structures have a variety of advantages and were intensively investigated for various photocatalytic applications.[29−34] However, few attentions have been paid to the potential of PWD using porous hollow structured semiconductor photocatalysts.[35] In this study, we synthesized highly porous fluorinated SnO_2 HNS in large-scale by the developed CIST methods. The integrated design of the oriented self-assembly and in situ self-transformation processes were highlighted for the formation mechanism. Moreover, these porous fluorinated SnO_2 HNS showed considerable activity in photocatalytic inactivation of a surface negatively charged, Gram-negative bacterium, *Escherichia coli* K-12, in aqueous

Received: October 29, 2013
Accepted: January 24, 2014
Published: January 24, 2014

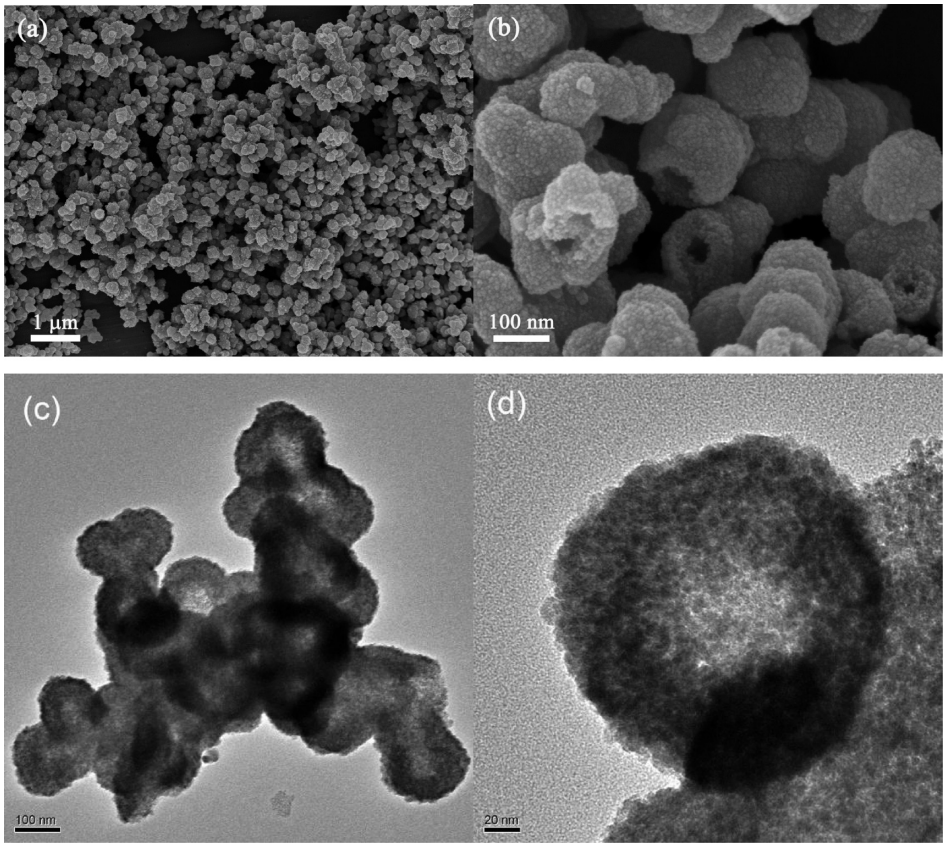

Figure 1. SEM (a, b) and TEM (c, d) images of SnO_2(F) HNS.

saline solution. The dominant reactive species involved in the inactivation process were also identified.

2. EXPERIMENTAL SECTION

2.1. Materials Preparations. Porous fluorinated SnO_2 hollow nanospheres (SnO_2(F) HNS) were prepared by a one-pot hydrothermal hydrolysis reaction of stannous fluoride (SnF_2) as a tin precursor in the presence of hydrogen peroxide (H_2O_2) as an adscititious oxidant. In a typical synthesis, 1.8 g (ca. 0.01 mol) of SnF_2 was added into 150 mL of aqueous solution containing sufficient H_2O_2 solution (5 mL, 30 wt %) under vigorous stirring. The resulting mixture was hydrothermally treated at 180 °C in a Teflon-lined stainless steel autoclave for 0−12 h. After reaction, the product was collected by centrifugation and then washed three times with distilled water to remove ionic impurities. Finally, the samples were dried at 65 °C in air. The as-obtained product was labeled as SnO_2(F) HNS. For comparison, additional samples were prepared by using $SnCl_2$ or $SnSO_4$ in place of SnF_2 under otherwise identical conditions to investigate the effects of anions in the tin precursors on the formation process of SnO_2(F) HNS. In addition, the effect of H_2O_2 as an oxidant on the formation process of SnO_2(F) HNS was also investigated in comparison with that using simply dissolved oxygen or ammonium persulfate ($(NH_4)_2S_2O_8$) as an adscititious oxidant.

2.2. Materials Characterization. Powder X-ray diffraction (XRD) patterns were obtained on a D/Max-RB X-ray diffractometer (Rigaku, Japan) using Cu Kα radiation at a scan rate of 0.05° 2θ s^{-1}. Scanning electron microscopy (SEM) was performed using a Hitachi-4800S microscope (Hitachi, Japan). Transmission electron microscopic (TEM) analysis was conducted using a Tecnai G^2 20S-TWIN microscope (FEI, Czech). The porous structure and Brunauer−Emmett−Teller (BET) surface area of the samples were analyzed by nitrogen sorption using a Micromeritics ASAP 2020 nitrogen adsorption apparatus (USA). X-ray photoelectron spectroscopic (XPS) measurements were conducted on a VG ESCALAB 210 electron spectrometer using Mg Kα radiation. XPS data were calibrated using the binding energy of C1s (285 eV) as the internal standard. The zeta potentials were measured by a zeta potential analyzer equipped with a data system of ZetaPlus 3.57 version and Model ZetaPlus (Brookhaven Instruments Corporation, NY, USA). The adsorption properties of the prepared SnO_2(F) HNS were evaluated in the dark at ambient temperature. Two azo dyes, methyl orange (MO) and methylene blue (MB), were selected as model adsorbates. Typically, 0.1 g of SnO_2(F) HNS was dispersed in a 20 mL mixed MO (6.5 mg/L) and MB (2.8 mg/L) aqueous solution in a 90 mm Petri dish. The selective decolorization process of MO and MB was monitored by a UV-2550 UV−visible spectrophotometer (Shimadzu, Japan). The photocatalytic generation of hydroxyl radicals ($^{\bullet}OH$) by the prepared SnO_2(F) HNS (50 mg) was investigated by photoluminescence (PL) method using terephthalic acid (5×10^{-4} mol/L, in 2×10^{-3} mol/L aqueous sodium hydroxide solution) as a probe molecule.[25] PL spectra of the generated 2-hydroxyterephthalic acid at specific time intervals (30 min) were measured on a fluorescence spectrophotometer (F-7000, Hitachi, Japan, excitation wavelength, 315 nm; fluorescence peak, 425 nm).

2.3. Photocatalytic Inactivation. A Gram-negative bacterium, *E. coli* K-12, was chosen as a model bacterium in this study. The experimental procedures are similar to those in our previous studies.[22−26,36] Typically, a suspension (100 mL) containing a specific photocatalyst (50 mg) and an *E. coli* K-12 (7.5×10^7 colony forming unit (cfu)/mL) in a beaker was placed in a black box and vigorously stirred by a magnetic stirrer at suitable velocity. The UV tube (λ_{max} = 365 nm, 15 W, 60 Hz, Cole-Parmer, USA) was chosen as the light source, the light intensity was measured by a UVX digital radiometer (UVP, Upland, CA, USA), and fixed at UVA, ca.1 mW/cm^2; UVB, ca. 0.7 mW/cm^2; UVC, ca. 0.05 mW/cm^2. All glassware used in the experiments was washed with deionized (DI) water, and then autoclaved at 121 °C for 20 min. *E. coli* K-12 was inoculated in 50 mL of nutrient broth (Lab M, Lancashire, U.K.) at 37 °C for 16 h in a shaking incubator. The bacterial cells were harvested by centrifugation

in an Eppendorf tube at 13,000 rpm for 1 min and washed twice with sterilized saline (0.9% NaCl) solution, and then resuspended in sterilized saline solution. The final cell density was adjusted to about 7.5×10^7 cfu/mL in the reaction mixture. At different time intervals, aliquots (typically, 1 mL) of the sample were collected and serially diluted with sterilized saline solution. 0.1 mL of the diluted sample was immediately spread on nutrient agar (Lab M, Lancashire, U.K.) plates and incubated at 37 °C for 24 h to determine the survival number of cells (in cfu). For comparison, dark (photocatalyst and bacterial cells without light), light (bacterial cells and light without photocatalyst) and negative controls (bacterial cells alone) were also included in the study. All treatment and control experiments were performed in triplicates. Each data point on the graphs represents the statistical results from these triplicate independent experiments, with a minimum of two samples examined for each experiment. These results are presented as mean values with standard deviations (i.e., the error bar of each data point). To identify the dominant reactive species (oxidative or charged) accounting for the inactivation of *E. coli* K-12, a specific scavenger at optimized concentration (elaborated in the caption of Figure 7) was added under otherwise identical conditions mentioned above.

The *E. coli* K-12 and SnO_2(F) HNS photocatalyst mixture was collected before and after photocatalytic treatment, and stained with the dyes of LIVE/DEAD *Bac*Light Bacterial Viability Kit (L7012, Molecular Probes, Inc., Eugene, OR) following the procedure recommended by the manufacturer. After incubation at 25 °C in the dark for 15 min, the samples were transferred to a coverslip and examined under a fluorescence microscopy (Nikon ECLIPSE 80i, Japan) equipped with a filter block NUV-2A consisting of excitation filter Ex 400−680 (Nikon, Japan) and Spot-K slider CCD camera (Diagnostic instruments. Inc., USA).

3. RESULTS AND DISCUSSION

3.1. Materials Synthesis and Characterization. The synthetic processes developed in the present study for SnO_2(F) HNS occurred spontaneously under mild hydrothermal conditions in aqueous solution containing stannous fluoride and hydrogen peroxide. The product obtained after aging at 180 °C for 12 h consisted of a high yield of nanospheres that were 100−200 nm in size (Figure 1). Interestingly, most of the nanospheres were in close contact with each other, often producing highly branched chains. A SEM image of broken nanospheres clearly revealed a hollow interior (Figure 1b). The shell walls, which consisted of loosely packed nanoparticles, appeared to be highly porous with a rough surface. TEM images of the hollow nanospheres indicated that the cavity diameter and shell wall thickness were approximately 50 and 40 nm, respectively (Figure 1c,d). These images also confirmed the presence of isolated discrete hollow spherical interiors and, in addition, indicated that the hollow nanospheres were often fused to give an "intestine-like" chambered interior cavity that was interconnected within the particle chains (Figure 1c,d). The high magnification TEM image of the external shell of individual nanospheres (Figure 1d) indicated that the walls were composed of numerous primary nanocrystals with sizes of 3−5 nm and their primary aggregates.

The apparent porous structure of the shell walls observed by SEM and TEM was confirmed by N_2 sorption analysis that gave a BET surface area (or S_{BET}) value of 156 $m^2\ g^{-1}$ and 47.5% porosity and showed nitrogen adsorption isotherms with a combination of type I and type IV behavior according to the IUPAC classification[37] (Figure 2). Interestingly, as indicated by the shape of the N_2 sorption curves and the corresponding pore size distribution (Figure 4Sa in the Supporting Information), the as-prepared hollow nanospheres were hierarchically porous, containing micropores, bimodal mesopores and macropores,

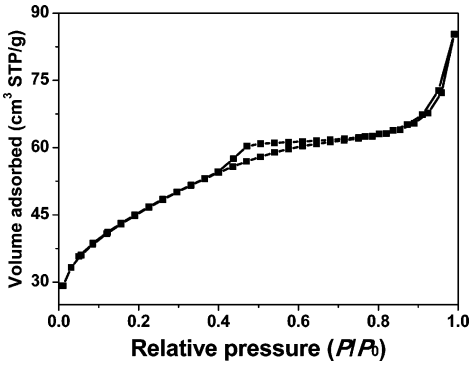

Figure 2. N_2 sorption isotherm of SnO_2(F) HNS.

which could be beneficial for photocatalytic reactions in a variety of aspects.

The powder XRD profile of these hollow SnO_2 microspheres showed reflections corresponding to phase-pure rutile (JCPDS No. 21-1250, Figure 1Sc, Supporting Information). Notably, as a result of the tiny crystallite size of primary nanobuilding blocks consisting of SnO_2 hollow nanospheres, the XRD peak intensities were obviously weak and the widths were significantly wider in comparison with the reference (JCPDS No. 21-1250). Using Scherrer's equation based on the (110) diffraction peak, the average crystallite size of was estimated to be about 4 nm, which was consistent with the TEM result. To further elucidate the chemical compositions and their electronic states, XPS analysis was carried out for those as-synthesized SnO_2(F) HNS. The XPS survey spectrum (data not shown) indicated that a trace amounts of F (ca. 3 atom %) was also detected in addition to Sn and O. The typical high resolution XPS spectra of Sn 3d and F 1s are presented in Figures 3a and 3b, respectively. Both Sn 3d peaks were highly symmetric, and the peak-to-peak separation of Sn 3d peaks was about 8.4 eV, which was close to that of reported value.[38,39] The peak corresponding to Sn $3d_{5/2}$ centered at 487.3 eV was ascribed to Sn^{4+}. Note that the binding energy corresponding to Sn $3d_{5/2}$ for SnO_2(F) was even larger than that for SnO_2 (486.5 eV) in the literature.[38,39] The high resolution XPS spectra of Sn 3d suggested that all the starting tin in +2 oxidation state was transformed into +4 oxidation states, during hydrothermal treatment in the presence of H_2O_2. Obviously, the F 1s peak centered at binding energies of about 684.7 was related to the F^- physically adsorbed on the surface.[40] Due to the higher electronegativity of F than that of O, surface fluorination shall account for an enhanced loss of electron density from Sn and the higher binding energy of Sn 3d in the as-prepared SnO_2(F) as mentioned above. The previous study[41] suggested that surface fluorination of semiconductor photocatalysts favored a variety of photocatalytic reactions, due to its combined effects on the surface adsorption as well as the charge separation and transfer dynamics.

3.2. Formation Processes and Mechanism of SnO_2 Hollow Nanospheres. To elucidate the time-dependent evolution processes of the porous SnO_2 hollow nanospheres, TEM and XRD analyses of the samples isolated from the reaction mixture maintained at 180 °C for various aging times were conducted. Samples collected prior to hydrothermal treatment (but after thorough mixing of stannous fluoride and hydrogen peroxide aqueous solution under vigorous stirring at ambient temperature for 3 h) consisted of interconnected amorphous and less-crystallized solid aggregates with diameters

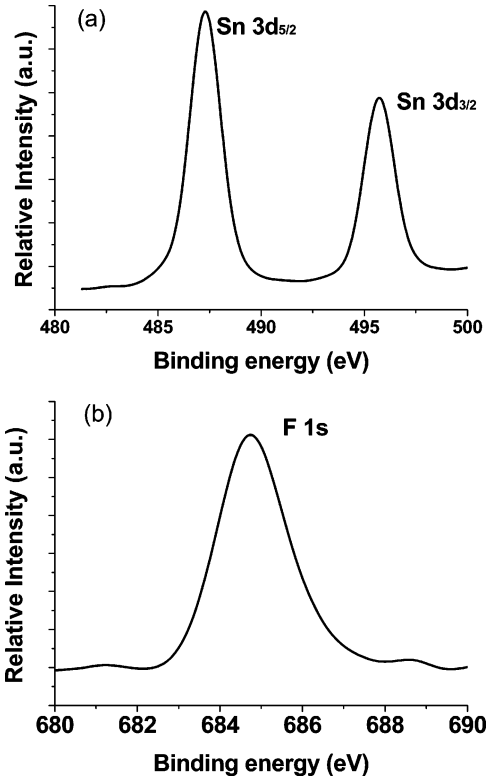

Figure 3. High-resolution XPS spectra of (a) Sn 3d and (b) F 1s profiles for SnO_2(F) HNS.

in the range of 100−200 nm (Figures 1Sa and 2Sa,b, Supporting Information). Few crystal grains were clearly separated. In the initial stage, the supersaturation of reaction system is high, and the explosive nucleation is dominant, which is followed by preferential spherical aggregation to reduce the overall Gibbs free energy because of the slow crystallization rate. Hydrothermal treatment of the mixture at 180 °C for 2 h resulted in the progressive transformation of the amorphous particles to crystalline SnO_2, as demonstrated by the obviously enhanced and resolved characteristic reflections in the XRD profiles (Figure 1Sb, Supporting Information). Corresponding TEM images (Figures 2Sc and 2Sd, Supporting Information) also indicated that well-separated crystal grains were evolved with obvious mesopores among them. It should be noticed that the initial stage of crystallization may occur especially on the external spherical surface, as indicated by the statistically larger crystal grains around crystalline shell wall (Figure 2Sd, Supporting Information). The nucleation rate is gradually reduced as the supersaturation falls with time in the surrounding solution; in contrast, the crystallization rate is progressively increased with increasing hydrothermal temperature. Consequently, the newly nucleated particles tend to evolve as well-crystallized ones before their deposition on the external surface of starting spherical aggregates. Meanwhile, the evacuation of the solid interior initiated at the core of some spherical aggregates (Figure 2Sd, Supporting Information) was observed. With further increases of the ripening time, evacuation of the particle interior became more pronounced, accompanied with increases in both the cavity diameter and degree of crystallinity (Figure 1c,d). This is associated with the localized Ostwald ripening processes, in which preferential dissolution of the amorphous or less-crystallized particle interior occurs to provide nutrients for continuous deposition of well-crystallized nanoparticles on the shell wall.

Overall, the formation of hollow SnO_2 nanospheres go through nonequilibrium transformative self-assembly processes,[42] that is, oriented self-assembly involving aggregation (and/or primary crystallization) after nucleation, and followed by in situ self-transformation characterized as localized dissolution and recrystallization (Scheme 1). For the successful

Scheme 1. Transformative Self-Assembly Processes Characterized for Forming SnO_2(F) HNS[a]

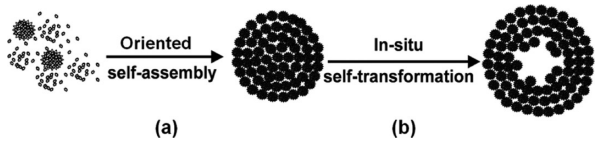

[a](a) Oriented self-assembly of the incipient amorphous (or less-crystallized) SnO_2 nanoclusters and/or their spontaneous primary aggregates into metastable spherical aggregates with solid form; (b) in situ self-transformation by matter relocation with regard to preferential dissolution of the metastable interior core and concurrently enhanced crystallization of the external shell involving localized inside-out Ostwald ripening.

formation of hollow SnO_2 nanospheres, delicated control of both of the above-involved processes is necessary. To reduce the overall Gibbs free energy, the aggregation (including primary and secondary aggregations) and primary crystallization (those resulting primary crystallites are still metastable and are doomed to subject to the subsequent dissolution and recrystallization processes) are two competitive but usually concurring processes following the initial nucleation. In the present study, the primary and secondary aggregation into metastable spherical assemblies is overwhelming in comparison with primary crystallization, which is determined largely by carefully selected chemical species in the designed reaction systems and reaction conditions. Specifically, the selection of tin fluoride as precursor is essential. When $SnCl_2$ was used instead of SnF_2, only well-dispersed tiny phase-pure SnO_2 nanocrystals were produced with the average grain size less than 10 nm (Figure 3Sa, Supporting Information, and Figure 4a,b). The relative weak complexing ability of chloride ions favor the faster primary crystallization process over the aggregation process after initial nucleation. In fact, the complexing anions usually affect the hydrolytic nucleation, aggregation, dissolution and recrystallization processes of metal oxide. In this study, the stronger complexing ability of fluoride ions facilitate the primary aggregation over crystallization and, significantly, also promote the dissolution of primary crystallite for recrystallization. The former contributes to oriented spherical organization, and the latter leads to directed evacuation. When $SnSO_4$ was used instead of SnF_2, a large portion of solid SnO_2 nanospheres were produced together with the hollow ones (Figure 3Sb, Supporting Information, and Figure 4c,d). The complexing-mediated dissolving ability of fluoride ions shall be stronger than that of sulfate ions, accelerating the hollowing rate, and giving rise to hollow SnO_2 nanospheres in higher portion than the solid ones at the specific hydrothermal reaction time. The effects of tin precursor on the crystallization and aggregation processes could also be reflected to some extent by the pore structures of the corresponding SnO_2 products. As shown in Figure 4S

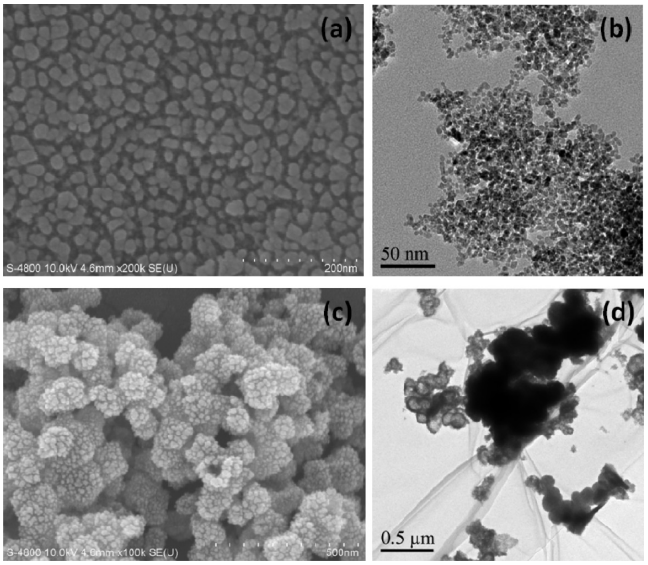

Figure 4. SEM (a, c) and TEM (b, d) images of SnO_2 samples prepared using $SnCl_2$ (a, b) or $SnSO_4$ (c, d) instead of SnF_2.

(Supporting Information), although monomodal mesopores were dominated for SnO_2 nanocrystals synthesized from $SnCl_2$, bimodal mesoporous structures were apparently resulted for SnO_2 structures synthesized from SnF_2 and $SnSO_4$. The bimodal mesopores can be largely related to primary and secondary aggregations, which give rise to finer intra-aggregated mesopores and larger interaggregated meso-/macropores, respectively. Note that the maximum pore diameter of interaggregated pores for hollow SnO_2 nanospheres from SnF_2 was about 50 nm (Figure 4Sa, Supporting Information), which was somewhat larger than that from $SnSO_4$, about 45 nm (Figure 4Sb, Supporting Information). The fluoride promoted hollowing of the interior space of SnO_2 nanospheres, in comparison to sulfate, shall contribute to the aforementioned variation.

In the present study, the selection of H_2O_2 is also crucial for the formation of porous SnO_2 nanospheres. The absence of H_2O_2 as an adscititious oxidant only resulted in multicomponent mixtures of partially reduced tin oxides in addition to SnO_2, as indicated by the corresponding XRD result (data not shown) and previous study.[43] The dissolved oxygen concentration in water is normally less than 0.3 mM (that is 9 mg/L, whereas our measured value is about 8 mg/L) under ambient conditions, which is far from enough for the full oxidation of Sn(II) at the designed concentration (ca. 75 mM). Although excessive ammonium persulfate ($(NH_4)_2S_2O_8$) was used as an adscititious oxidant instead of H_2O_2, pure SnO_2 can be obtained; the obtained products were mainly solid spheres with nonuniform particle size (Figure 5S, Supporting Information). This result indicates that the added H_2O_2 not only acts as oxidant but also contributes to oriented spherical organization during aggregation process and the preferential dissolution during recrystallization process (also the hollowing process).

3.3. Performance and Mechanism of Photocatalytic Bacterial Inactivation. The as-prepared SnO_2(F) HNS had typical light absorption in the UV region with an absorption tail up to 400 nm (Figure 6S, Supporting Information). The band gap related to direct allowed transition was estimated to be ca. 4.2 eV based on the intercept of the tangent of the plot of $(Ah\nu)^2$ versus $h\nu$, which was much larger than that of bulk SnO_2, usually 3.6 eV. When the tiny crystallite size (3−5 nm) of the primary nanobuilding blocks of the as-prepared SnO_2(F) HNS is taken into account, quantum effect may be responsible for such a wider band gap. A wider band gap was usually indicative of higher photocatalytic redox ability, and the generation of hydroxyl radical ($^{\bullet}OH$) under UV irradiation was detected as a confirmation. As shown in Figure 7S (Supporting Information), the fluorescence intensity corresponding to generated 2-hydroxyterephthalic acid was increasingly enhanced with prolonging irradiation time, indicating that the $^{\bullet}OH$ was progressively generated upon light excitation of SnO_2(F) HNS.

As documented, the surface fluorination usually does not affect the optical absorption properties, but it affects the charge separation and transfer dynamics as well as the surface adsorption properties.[41] The isoelectric point (zero point of zeta potential) of SnO_2 is normally close to pH 4.3,[44] which implies that the surface of SnO_2 is negatively charged in neutral aqueous solution. As the surface fluorination usually further reduces the surface charge,[41] it is expected that the as-prepared SnO_2(F) HNS shall also be negatively charged. Such an assumption was readily confirmed by the measured zeta potential of their suspension in DI water, which is ca. −45 mV. Moreover, the surface negative charge of as-prepared SnO_2(F) hollow nanospheres was also demonstrated by the highly selective dye adsorption toward positively charged MB rather than negatively charged MO (Figure 8S, Supporting Information).

Unfortunately, the cell surface of *E. coli* K-12 is negatively charged in neutral aqueous solution, which shall repel the negatively charged SnO_2(F) HNS as a photocatalyst. The incurring inhibited interfacial contact is supposed to be disadvantageous more or less for the photocatalytic inactivation process. Surprisingly, the SnO_2(F) hollow nanospheres as a photocatalyst were quite effective in inactivating the *E. coli* K-12, with 7.5×10^7 cfu/mL of cells being inactivated frequently in less than 150 min (Figure 5c). The interaction between SnO_2(F) HNS and *E. coli* K-12 was probably enhanced in saline (0.9% NaCl) solution due to the reduced interfacial repulsion force. High ionic strength of solution usually cause the electrical double layer compression, in fact, the measured zeta potential of suspension of SnO_2(F) HNS in saline solution was sharply

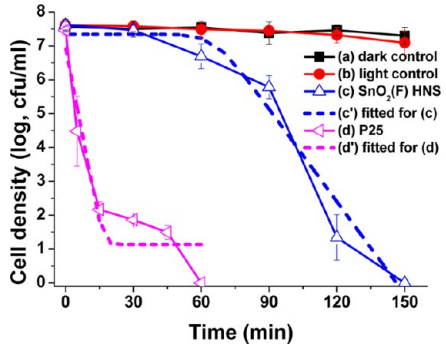

Figure 5. The photocatalytic inactivation of *E. coli* K-12 using porous SnO_2(F) HNS (c) versus Degussa P25 (d) as a photocatalyst. No significant inactivation occurs in the dark (a) and light (b) controls. (c′) and (d′) are the fitted curves for (c) and (d), respectively, and the fitted parameters: k_{max} = 0.21 min^{-1}, S = 66 min, and R^2 = 0.96 for (c), k_{max} = 0.80 min^{-1}, N_{res} = 1.14 (log, cfu/mL), R^2 = 0.91 for (d).

dx.doi.org/10.1021/am4047975 | ACS Appl. Mater. Interfaces 2014, 6, 2407−2414

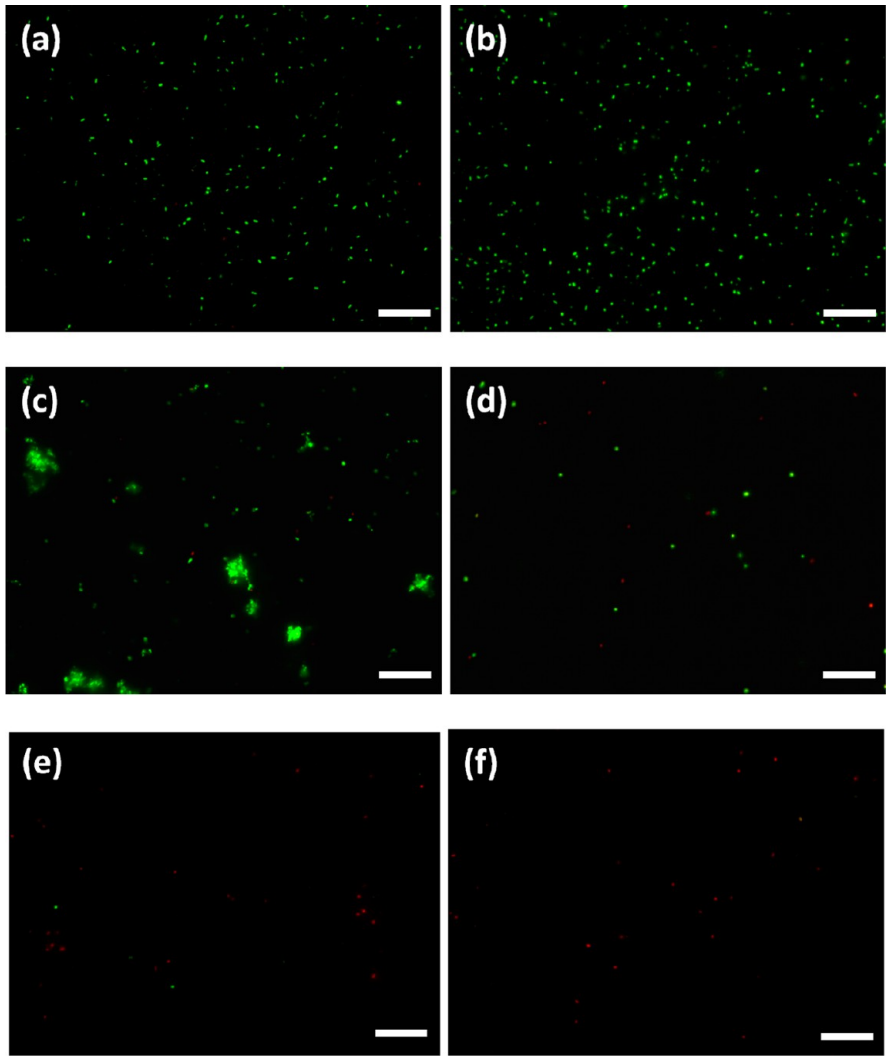

Figure 6. Fluorescence microscopic images of *E. coli* K-12 (7.5×10^7 cfu/mL, 100 mL) photocatalytically untreated or treated in the presence of SnO_2(F) HNS as a photocatalyst (50 mg). (a) *E. coli* K-12. (b) The mixture of SnO_2(F) HNS and *E. coli* K-12 before irradiation, and after irradiation for (d) 1, (e) 3, and (f) 6 h. (c) The control mixture Evonik Degussa P25 and *E. coli* K-12 before irradiation. The scale bars are 20 μm.

reduced to ca. −0.9 mV. As a comparison, the dark control was carried out with the SnO_2(F) HNS in dark, whereas the light control was carried out in the absence of any photocatalyst under identical UV irradiation. In both light and dark control experiments, the bacterial population remained almost unchanged, with normally less than 0.5 log reduction after 150 min (Figure 5a,b), suggesting no significant toxic effect of the used photocatalysts and no appreciable photolysis happened to *E. coli* K-12. In this connection, it is indicated that the photocatalytic effects account for the effective inactivation of *E. coli* K-12 in the present inactivation system.

To further confirm the bactericidal effect of SnO_2(F) HNS as a photocatalyst, the *Bac*Light Kit fluorescent microscopic method was conducted according to previous studies.[22,26] In principle, live bacterial cells with intact cell membranes are stained by green fluorescence dye, whereas dead bacterial cells with damaged cell membranes are stained by red fluorescence dye.[22,26] As shown in Figure 6a, the photocatalytically untreated bacteria exhibited intense green fluorescence. Notably, the SnO_2(F) HNS photocatalyst could not been stained by both dyes, and there was no intense interaction between cells and the SnO_2(F) HNS photocatalyst (Figure 6b), which was in sharp contrast to the serious aggregation of bacteria in the presence of Evonik Degussa P25 (a landmark photocatalyst containing mixed-phase TiO_2) (Figure 6c). After photocatalytically treatment for 1 h, a portion of bacteria exhibited red fluorescence (Figure 6d), indicating a loss of cell membrane integrity (or alteration in membrane permeability). As the irradiation time was prolonged, increasingly more red stained bacterial cells were observed (Figure 6e,f). Therefore, it was concluded that the SnO_2(F) photocatalyst performed progressive damage on the bacterial cell membrane and had a considerable photocatalytic inactivation effect.

Admittedly, the photocatalytic inactivation efficiency of the as-prepared SnO_2(F) HNS was still unsatisfying, especially as compared to the Degussa P25, which completely inactivated 7.5×10^7 cfu/mL of *E. coli* K-12 within 60 min (Figure 5d). Moreover, their inactivation kinetics were somewhat different from each other. It was suggested that the photocatalytic inactivation of *E. coli* probably involved three characteristic stages: (a) the initial shoulder phase, (b) the main bacteria inactivation period, and (c) the final tailing stage.[45] A tailing may occur because of lysis of damaged cells, with the liberated intracellular components acting as competitors against the

intact cells for the photocatalytic attack, while a shoulder is reasoned by a cumulative damage through photocatalytic redox reactions before a single cell was completely inhibited from the proliferation. In our study, the tailing stage was negligible for inactivation process using as-prepared SnO_2(F) HNS as a photocatalyst, while the shoulder phase was skipped off by Degussa P25-mediated photocatalytic inactivation process. The inactivation kinetics can be well fitted by a model proposed by Geeraerd et al.[45] Specifically, the inactivation kinetics can be fitted by the eq 1 (the typical "shoulder + log−linear" model) for the case using as-prepared SnO_2(F) HNS as a photocatalyst:

$$N(t) = N_0 e^{-k_{max}t} \frac{e^{k_{max}S}}{1 + (e^{k_{max}S} - 1)e^{-k_{max}t}} \quad (1)$$

In contrast, the inactivation kinetics can be fitted by the eq 2 for the case using Degussa P25 as a photocatalyst:

$$N(t) = (N_0 - N_{res})e^{-k_{max}t} + N_{res} \quad (2)$$

In both equations, the $N(t)$ and N_0 were related to the survival number of cells (log, in cfu) at irradiation time equal to t and 0, respectively; k_{max} denoted the inactivation rate; S was the shoulder length (time span of initial incubation phase) and N_{res} was the tail height, that is, residual number of cells (log, in cfu). The number e was the base of the natural logarithm, approximately equal to 2.71828. The fitted results were shown in Figure 5. And especially, the fitted parameters k_{max} = 0.21 min^{-1}, S = 66 min, and R^2 = 0.96 are reported for inactivation process using as-prepared SnO_2(F) HNS as a photocatalyst based on the above-mentioned shoulder + log−linear model.

The different inactivation kinetics, using as-prepared SnO_2(F) HNS versus Degussa P25 as the different photocatalysts, reflected their different inactivation mechanisms. Among others, an identification of the dominant photogenerated reactive species is one of the most important steps toward understanding the inactivation mechanism. In this study, a scavenger study was applied to identify the major photogenerated reactive species responsible for the inactivation of the *E. coli* K-12 using as-prepared SnO_2(F) HNS as the photocatalyst. As shown in Figure 7, with the addition of isopropanol or 4-hydroxy-2,2,6,6-tetramethylpiperidinyloxy (TEMPOL) as a scavenger for the hydroxyl radical ($^{\bullet}OH$) or superoxide ($^{\bullet}O_2^-$), respectively, no significant change in the inactivation efficiency was observed as compared with that without any scavenger (Figures 7b,c), implying that both $^{\bullet}OH$ and $^{\bullet}O_2^-$ were not the major reactive species accounting for the inactivation process using as-prepared SnO_2(F) HNS as the photocatalyst. The minor role of $^{\bullet}O_2^-$ is expected, as the production of $^{\bullet}O_2^-$ is thermodynamically forbidden as a result of the lowest conduction band position of SnO_2 relative to the redox potential for one-electron reduction of O_2 into $^{\bullet}O_2^-$ (−0.046 V vs SHE). However, no contribution to bacterial inactivation from $^{\bullet}OH$ was surprising, as production of $^{\bullet}OH$ was thermodynamically favored and was detected, as demonstrated in Figure 7S (Supporting Information). Although further confirmation is still required, short lifetime and short diffusion distance of highly reactive $^{\bullet}OH$ probably discounts the effect of $^{\bullet}OH$. It is possible that the short-lived $^{\bullet}OH$ is quenched or is converted to relatively stable reactive species (such as H_2O_2) before enough $^{\bullet}OH$ is enriched for a complete damage of a single cell. The contribution from H_2O_2 was affirmed by the significant decrease in the inactivation efficiency after adding Fe(II)-EDTA in the photocatalytic system as the scavenger of H_2O_2 (Figure 7e). Thermodynamically, H_2O_2 can be generated by either two-electron reduction of surface adsorbed O_2 (0.68 V vs SHE) or two-electron oxidation of surface adsorbed H_2O (1.78 V vs SHE). Similarly, the importance of hole (h^+) was also determined by the great decrease in the inactivation efficiency after adding sodium oxalate as scavenger of h^+ (Figure 7d). However, the role of electron (e^-) was still unclear, after adding Cr(VI) as the scavenger of e^-, the inactivation efficiency was otherwise significantly enhanced (Figure 7f). The toxic effects of Cr(VI) cannot account for such a great variation, as confirmed by the corresponding dark and light control (Figures 7g,h). It is supposed that the consumption of e^- by Cr(VI) as the scavenger would significantly enhance the hole−electron separation efficiency and thus favor the inactivation process mediated by the holes or their derived hydrogen peroxide. Overall, the photogenerated h^+ and H_2O_2 are suggested as the dominant effective reactive species in the present system.

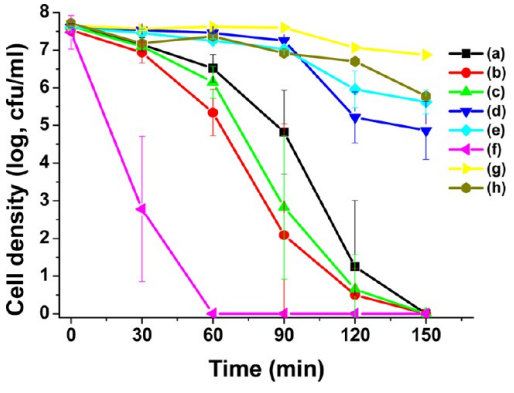

Figure 7. The photocatalytic inactivation of *E. coli* K-12 with SnO_2(F) HNS in the presence of different scavengers: (a) no scavenger, (b) 5 mM isopropanol, (c) 2 mM TEMPOL, (d) 0.5 mM sodium oxalate, (e) 0.1 mM Fe(II)-EDTA and (f) 0.05 mM Cr(VI). (g, h) Dark and light controls for (f), respectively.

4. CONCLUSIONS

Highly porous surface fluorinated SnO_2 hollow nanospheres are produced in high yield based on the CIST method. Their formation mainly involves the oriented self-assembly and in situ self-transformation processes, which are demonstrated to be well controlled by the directing effects of selected specific chemical species (stannous fluoride as tin precursor and hydrogen peroxide as oxidant) in the present synthesis system. Significantly, these porous fluorinated SnO_2 hollow nanospheres show considerable activity in photocatalytic inactivating surface negatively charged Gram-negative bacterium, *Escherichia coli* K-12, in aqueous saline solution, and the inactivation kinetics can be well fitted using the typical shoulder + log−linear model. Although the complex bacterial inactivation processes and mechanism required more detailed investigations, based on the scavenger studies, H_2O_2 and photogenerated h^+ are suggested as the major reactive species responsible for the bacterial inactivation process in the present photocatalytic system.

■ ASSOCIATED CONTENT

Supporting Information

Additional detail information including XRD, SEM, TEM and pore size distribution results (Figures 1S−5S) of control experiments for investigating formation processes and mechanism, as well as optical properties (Figure 6S), detection of photogenerated hydroxyl radicals (Figure 7S) and adsorption selectivity (Figure 8S). This material is available free of charge via the Internet at http://pubs.acs.org.

■ AUTHOR INFORMATION

Corresponding Authors

*J. G. Yu. Tel: +86 27 8787 9468. Fax: +86-27-87879468. E-mail: jiaguoyu@yahoo.com.

*P. K. Wong. Tel: +852 3943 6383. Fax: +852 2603 5767. E-mail: pkwong@cuhk.edu.hk.

Notes

The authors declare no competing financial interest.

■ ACKNOWLEDGMENTS

The support of Hong Kong Scholars Program (XJ2012037), Postdoctoral Science Foundation of China (2012T50690, 2013M531751) and NSFC (21103131) to S.W. Liu are gratefully acknowledged. The project was also financially supported by a research grant (GRF476811) of the Research Grant Council, Hong Kong SAR Government to P. K. Wong, and research grants of the NSFC (51272199, 51320105001), 973 Program (2013CB632402, 2010CB923200), and 863 Program (2012AA062701) to J. G. Yu.

■ REFERENCES

(1) Lou, X. W.; Archer, L. A.; Yang, Z. C. *Adv. Mater.* **2008**, *20*, 3987−4019.

(2) Hu, J.; Chen, M.; Fang, X. S.; Wu, L. W. *Chem. Soc. Rev.* **2011**, *40*, 5472−5491.

(3) Lou, X. W.; Wang, Y.; Yuan, C. L.; Lee, J. Y.; Archer, L. A. *Adv. Mater.* **2006**, *18*, 2325−2329.

(4) Wang, C. H.; Chu, X. F.; Wu, M. M. *Sens. Actuators, B* **2007**, *120*, 508−513.

(5) Qian, J. F.; Liu, P.; Xiao, Y.; Jiang, Y.; Cao, Y. L.; Ai, X. P.; Yang, H. X. *Adv. Mater.* **2009**, *21*, 3663−3667.

(6) Shi, L. A.; Lin, H. L. *Langmuir* **2010**, *26*, 18718−18722.

(7) Zhao, Q. R.; Xie, Y.; Dong, T.; Zhang, Z. G. *J. Phys. Chem. C* **2007**, *111*, 11598−11603.

(8) Wu, P.; Du, N.; Zhang, H.; Zhai, C. X.; Yang, D. R. *ACS Appl. Mater. Interfaces* **2011**, *3*, 1946−1952.

(9) Ding, S. J.; Chen, J. S.; Qi, G. G.; Duan, X. N.; Wang, Z. Y.; Giannelis, E. P.; Archer, L. A.; Lou, X. W. *J. Am. Chem. Soc.* **2011**, *133*, 21−23.

(10) Zhong, Z. Y.; Yin, Y. D.; Gates, B.; Xia, Y. N. *Adv. Mater.* **2000**, *12*, 206−209.

(11) Lou, X. W.; Yuan, C. L.; Archer, L. A. *Adv. Mater.* **2007**, *19*, 3328−3332.

(12) Wang, Z. Y.; Luan, D. Y.; Boey, F. Y. C.; Lou, X. W. *J. Am. Chem. Soc.* **2011**, *133*, 4738−4741.

(13) Wang, W. W.; Zhu, Y. J.; Yang, L. X. *Adv. Funct. Mater.* **2007**, *17*, 59−64.

(14) Yin, X. M.; Li, C. C.; Zhang, M.; Hao, Q. Y.; Liu, S.; Chen, L. B.; Wang, T. H. *J. Phys. Chem. C* **2010**, *114*, 8084−8088.

(15) Wang, H. K.; Fu, F.; Zhang, F. H.; Wang, H. E.; Kershaw, S. V.; Xu, J. Q.; Sun, S. G.; Rogach, A. L. *J. Mater. Chem.* **2012**, *22*, 2140−2148.

(16) Yang, H. G.; Zeng, H. C. *Angew. Chem., Int. Ed.* **2004**, *43*, 5930−5933.

(17) Yu, J. G.; Guo, H. T.; Davis, S. A.; Mann, S. *Adv. Funct. Mater.* **2006**, *16*, 2035−2041.

(18) Yu, H. G.; Yu, J. G.; Liu, S. W.; Mann, S. *Chem. Mater.* **2007**, *19*, 4327−4334.

(19) Cai, W. Q.; Yu, J. G.; Mann, S. *Microporous Mesoporous Mater.* **2009**, *122*, 42−47.

(20) Liu, S. W.; Yu, J. G.; Mann, S. *Nanotechnology* **2009**, *20*, 325606 (7pp).

(21) Yu, X. X.; Yu, J. G.; Cheng, B.; Huang, B. B. *Chem. − Eur. J.* **2009**, *15*, 6731−6739.

(22) Zhang, L. S.; Wong, K. H.; Yip, H. Y.; Hu, C.; Yu, J. C.; Chan, C. Y.; Wong, P. K. *Environ. Sci. Technol.* **2010**, *44*, 1392−1398.

(23) Chen, Y. M.; Lu, A. H.; Li, Y.; Zhang, L. S.; Yip, H. Y.; Zhao, H. J.; An, T. C.; Wong, P. K. *Environ. Sci. Technol.* **2011**, *45*, 5689−5695.

(24) Wang, W. J.; Zhang, L. Z.; An, T. C.; Li, G. Y.; Yip, H. Y.; Wong, P. K. *Appl. Catal., B* **2011**, *108*, 108−116.

(25) Wang, W. J.; Yu, Y.; An, T. C.; Li, G. Y.; Yip, H. Y.; Yu, J. C.; Wong, P. K. *Environ. Sci. Technol.* **2012**, *46*, 4599−4606.

(26) Xia, D. H.; Ng, T. W.; An, T. C.; Li, G. Y.; Li, Y.; Yip, H. Y.; Zhao, H. J.; Lu, A. H.; Wong, P. K. *Environ. Sci. Technol.* **2013**, *47*, 11166−11173.

(27) Zhang, D. Q.; Li, G. S.; Yu, J. C. *J. Mater. Chem.* **2010**, *20*, 4529−4536.

(28) Wang, W. J.; Yu, J. C.; Wong, P. K. In *Photocatalytic Materials & Surfaces for Environmental Cleanup-II*; Tayade, R. J., Ed.; Trans Tech Publications Ltd.: Stafa-Zurich, Switzerland, 2013; Vol. *734*, pp 63−89.

(29) Yu, J. G.; Liu, S. W.; Yu, H. G. *J. Catal.* **2007**, *249*, 59−66.

(30) Li, H. X.; Bian, Z. F.; Zhu, J.; Zhang, D. Q.; Li, G. S.; Huo, Y. N.; Li, H.; Lu, Y. F. *J. Am. Chem. Soc.* **2007**, *129*, 8406−8407.

(31) Pan, J. H.; Zhang, X. W.; Du, A. J.; Sun, D. D.; Leckie, J. O. *J. Am. Chem. Soc.* **2008**, *130*, 11256−11257.

(32) Yu, J. G.; Yu, H. G.; Guo, H. T.; Li, M.; Mann, S. *Small* **2008**, *4*, 87−91.

(33) Yu, J. G.; Yu, X. X. *Environ. Sci. Technol.* **2008**, *42*, 4902−4907.

(34) Yu, J. G.; Yu, X. X.; Huang, B. B.; Zhang, X. Y.; Dai, Y. *Cryst. Growth Des.* **2009**, *9*, 1474−1480.

(35) Pang, M. L.; Hu, J. Y.; Zeng, H. C. *J. Am. Chem. Soc.* **2010**, *132*, 10771−10785.

(36) Gao, M. H.; An, T. C.; Li, G. Y.; Nie, X.; Yip, H. Y.; Zhao, H.; Wong, P. K. *Water Res.* **2012**, *46*, 3951−3957.

(37) Sing, K. S. W.; Everett, D. H.; Haul, R. A. W.; Moscou, L.; Pierotti, R. A.; Rouquerol, J.; Siemieniewska, T. *Pure Appl. Chem.* **1985**, *57*, 603−619.

(38) Yu, J. G.; Liu, S. W.; Zhou, M. H. *J. Phys. Chem. C* **2008**, *112*, 2050−2057.

(39) *Handbook of X-ray Photoelectron Spectroscopy*; Moulder, J. F., Stickle, W. F., Sobol, P. E., Bomben, K. D., Chastain, J., Eds.; Pekin-Elmer Inc., Physical Electronics Division: Eden Prairie, MN, 1992.

(40) Yu, J. C.; Yu, J. G.; Ho, W. K.; Jiang, Z. T.; Zhang, L. Z. *Chem. Mater.* **2002**, *14*, 3808−3816.

(41) Liu, S. W.; Yu, J. G.; Cheng, B.; Jaroniec, M. *Adv. Colloid Interface Sci.* **2012**, *173*, 35−53.

(42) Mann, S. *Nat. Mater.* **2009**, *8*, 781−792.

(43) Wang, C.; Du, G. H.; Stahl, K.; Huang, H. X.; Zhong, Y. J.; Jiang, J. Z. *J. Phys. Chem. C* **2012**, *116*, 4000−4011.

(44) Xu, Y.; Schoonen, M. A. A. *Am. Mineral.* **2000**, *85*, 543−556.

(45) Geeraerd, A. H.; Herremans, C. H.; van Impe, J. F. *Int. J. Food Microbiol.* **2000**, *59*, 185−209.